Available online at www.sciencedirect.com
ScienceDirect
Trans. Nonferrous Met. Soc. China 33(2023) 2471−2482
Transactions of Nonferrous Metals Society of China
www.tnmsc.cn

Preparation of hollow core-shelled $MnCoSe_x$/MnO@nitrogen-doped carbon composite by multiple interfaces coupling and its electrochemical properties

Ji ZHOU[1], Li-na ZHANG[2], Bin-bin LIU[1], Cai-xia XU[1], Hong LIU[1,3]

1. Institute for Advanced Interdisciplinary Research (iAIR), University of Jinan, Jinan 250022, China;
2. Shandong Provincial Key Laboratory of Preparation and Measurement of Building Materials, University of Jinan, Jinan 250022, China;
3. State Key Laboratory of Crystal Materials, Shandong University, Jinan 250100, China

Received 8 March 2022; accepted 13 June 2022

Abstract: Hollow $MnCoSe_x$/MnO nanospheres wrapped with nitrogen-doped carbon shell ($MnCoSe_x$/MnO@N-C) were prepared via a simple solvothermal and selenization strategy followed by the carbon coating procedure. Benefitting from the multiple interfaces coupling between $MnCoSe_x$ and MnO and unique hollow core-shell architecture, $MnCoSe_x$/MnO@N-C composites possess high specific capacitance and superior rate capability, even at a high current density of 5 A/g, the $MnCoSe_x$/MnO@N-C can operate steadily for 20000 cycles with 84.6% of initial specific capacitance maintained. An asymmetric supercapacitor device assembled by $MnCoSe_x$/MnO@N-C and active carbon depicts a high energy density of 11.2 W·h/kg at a power density of 810 W/kg and a long cycle life with 84.0% of the initial specific capacitance retained after 20000 cycles.

Key words: selenides; hollow nanospheres; nitrogen-doped carbon; cathode; supercapacitor; electrochemical properties

1 Introduction

Considerable research has been conducted to search for eco-friendly and highly-efficient electrochemical energy storage systems [1−5]. Supercapacitors, as one class of promising and competitive devices, have drawn widespread focus thanks to numerous advantages of high power density, superior rate capability, long cycle life as well as clean features [6,7]. Supercapacitors are mainly classified into electric double-layer capacitors (EDLCs) through physical adsorption and pseudocapacitors based on reversible Faradaic redox reaction in accordance to the charge storage mechanisms [8,9]. The latter delivers higher specific capacitances compared to EDLCs [8,10]. Consequently, continuous efforts have been devoted to developing various kinds of pseudocapacitive electrode materials for high performance supercapacitors.

In recent years, transition metal oxides have been deeply explored as efficient redox-active electrode materials for electrochemical supercapacitors [7,11−13], yet their inferior electronic conductivity and stability hinder their practical applications [8,14]. Transition metal selenides owned much lower resistance due to higher electronic conductivity of Se (1×10^{-3} S/m) [14,15], which perform evident advantages as cathode materials for supercapacitors [16−19]. Of note, bimetallic selenides can further modify the respective electronic conductivity and generate the multiple redox reactions, thus synergistically

Corresponding author: Cai-xia XU, Tel: +86-531-82767046, E-mail: chm_xucx@ujn.edu.cn
DOI: 10.1016/S1003-6326(23)66274-0

enhancing the rate capacity [8,20−22]. Co-based selenides have won the special concern due to their higher intrinsic conductivity and splendid electrochemical properties [20]. Moreover, Mn-based selenides possess theoretically high conductivity but are often neglected as promising electrode material for energy storage [23]. As stated above, it is inspired to engineering MnCo-based selenides with the aim to further boost their charge storage performances in supercapacitors.

Besides the optimization of active components, nanostructure design is also an efficient way to alleviate the particle pulverization and structural destruction during charge−discharge process [22,24]. Among various nanostructures, the hollow nanostructure with abundant electrochemical active sites and large specific surface area can shorten the ion/electron diffusion lengths as well as mitigate the structural change [22,24−26]. In addition, coating highly conductive carbon-based material has been proved to be highly valid in preventing the structural pulverization [27]. Particularly, nitrogen-doped carbon is preferable to generating rich defects, enhancing the electronic conductivity, as well as improving the specific capacitance and cycling stability, accordingly resulting in optimized electrochemical performance [28,29].

Motivated by the statements above, we focus on the preparation of N-doped carbon wrapped hollow $MnCoSe_x$/MnO nanospheres via a facile hydrothermal process to obtain hollow $MnCo_2O_4$ nanospheres as the precursor followed by an incomplete selenization strategy and encapsulation of one protective carbon shell. Intercrossing $MnCoSe_x$ and MnO phases can generate rich interfaces and modify the electron structure, which is beneficial to providing multiple redox reactions and improving the mass transport. The hollow sphere configuration with high specific surface area can reduce the ion/electron diffusion pathway and relieve the structural destroy during the long-term charge storage process. Furthermore, the N-doped carbon layer wrapped on the surface of $MnCoSe_x$/MnO as a robust protective shell can not only improve the electrical conductivity but also strengthen the structure stability. As is expected, $MnCoSe_x$/MnO@N-C electrode exhibits high specific capacitance, excellent rate capability, and superior cycling performances. The asymmetric supercapacitor (ASC) device assembled by $MnCoSe_x$/MnO@N-C and active carbon (AC) displays high energy density, outstanding rate capability, and exceptional cycling stability. Owing to the great performances and convenient preparation, $MnCoSe_x$/MnO@N-C electrode shows substantial application potential as an advanced cathode material for supercapacitors.

2 Experimental

2.1 Sample preparation

2.1.1 Synthesis of $MnCo_2O_4$ hollow spheres

In the typical preparation, 0.3 g polyvinyl pyrrolidone (PVP, K30) was dispersed into 38 mL ethylene glycol (EG) under rigorous stirring. Subsequently, 498.16 mg $Co(CH_3COO)_2·4H_2O$ and 245.09 mg $Mn(CH_3COO)_2·4H_2O$ were dissolved into the above solution and refluxed at 170 °C for 1 h to obtain purple viscous solution and then directly transferred into a Teflon-lined stainless steel autoclave at 155 °C for 10 h. Finally, the dark purple precipitate was separated by filtration, washed with ethanol and dried at 60 °C. All the reagents were of analytical purity and used without further purification.

2.1.2 Synthesis of $MnCoSe_x$/MnO hollow spheres

55.48 mg SeO_2 was dispersed into 15 mL EG solution and then 5 mL $N_2H_4·H_2O$ was added to obtain a homogeneous red solution. After that, 39 mg $MnCo_2O_4$ obtained above was dispersed in the red solution with continuous stirring and then transferred into autoclave and further kept at 140 °C for 10 h. The resulting black product was collected via centrifugation, and finally dried in the vacuum at 60 °C.

2.1.3 Synthesis of $MnCoSe_x$/MnO@N-C composites

60 mg $MnCoSe_x$/MnO sample was dispersed into 30 mL HCl/tris-buffer solution under ultra-sonication followed by the addition of 20 mg dopamine hydrochloride by stirring for another 24 h. The products were centrifuged and dried at 60 °C. Subsequently, the black solid was calcined at 600 °C for 2 h with a heating rate of 5 °C/min under Ar atmosphere.

2.2 Material characterization

The crystal structures of all samples were studied via powder X-ray diffraction (XRD)

(Bruker D8, Cu K_α). The chemical state was analyzed by X-ray photoelectron spectroscopy (XPS) (ESCALAB 250). Raman data were recorded by Raman spectrometer (HORIBA Jobin YvonT-64000) under an excitation wavelength of 532 nm. The morphologies of the samples were characterized via transmission electron microscope (TEM) (JEM−2100F) and scanning electron microscope (SEM) (JEOL JSM−6700) with an X-sight energy dispersive X-ray spectrometer (EDS) (Oxford INCA) for the compositional analysis.

2.3 Electrode preparation and electrochemical tests

The working electrodes were fabricated by mixing 80 wt.% $MnCoSe_x$/MnO@N-C ($MnCoSe_x$/MnO or $MnCo_2O_4$), 10 wt.% Super P, and 10 wt.% polyvinylidene fluoride (PVDF) with an appropriate amount of N-methy-l-2-pyrrolidine solvent. The slurry was then coated onto a nickel foam current collector with the mass loading at about 8 mg/cm^2, and dried overnight at 80 °C followed by being pressed at 10.0 MPa for several seconds. The electrochemical performances were tested on the electrochemical workstation (CHI 760E). In the three-electrode system, 6 mol/L KOH was utilized as the electrolyte with a Pt foil as the counter electrode and a Hg/HgO electrode as the reference electrode. The cyclic voltammetry (CV) and galvanostatic charge−discharge (GCD) tests were implemented in the potential window of 0−0.55 V. Electrochemistry impedance spectroscopy (EIS) was recorded in the frequency range from 0.01 to 100 kHz. In addition, two-electrode asymmetric device was constructed by using AC coated on the nickel foam as the negative electrode, filter paper as the separator, and 1 mol/L KOH solution as the electrolyte, respectively. The mass loading values of the $MnCoSe_x$/MnO@N-C and AC electrodes in the asymmetric device were kept at 6.2 and 2.24 mg/cm^2, respectively, in accordance with the charge balance theory (Q_+=Q_-) [9]:

$$Q=C\Delta Vm$$

where Q is the quantity of electric charge, C is the specific capacitance, ΔV is the potential window, and m is the mass loading. The calculation formulas of specific capacitance, energy density, and power density are given in Eqs. S(1)−(3), respectively in Supplementary Materials (SM).

3 Results and discussion

3.1 Morphology and structure

The preparation process of hollow $MnCoSe_x$/MnO@N-C nanosphere is illustrated in Fig. 1. First, PVP acts as the soft template with the strong coordination ability towards Co^{2+} and Mn^{2+}, and solid MnCo-glycolate sphere was produced upon refluxing at 170 °C for 1 h. According to the well-known Ostwald ripening process [30,31], the solid sphere eventually evolves into the hollow spherical $MnCo_2O_4$ precursor after the solvothermal reaction. After that, the hollow $MnCoSe_x$/MnO sphere was obtained through incomplete selenization. Eventually, the coating with polydopamine and carbonizing at 600 °C resulted in the hollow $MnCoSe_x$/MnO@N-C nanosphere. EDS data of all samples are provided in Fig. S1 in SM. In the $MnCo_2O_4$ precursor (Fig. S1(a)), the atomic ratio of Mn and Co was 17.1: 33.8, almost closing to 1:2. After selenization (Fig. S1(b)), the atomic ratio of Mn, Co, and Se is about 9.9:19.6:55.9, indicating that the bimetallic ratio is well maintained and the selenide is successfully prepared. After carbon coating (Fig. S1(c)), the atomic ratio of Mn, Co, and Se maintained at 12.9:25.56:48.76, demonstrating that carbonization process does not change the initial constituents of the product.

The structural evolution from $MnCo_2O_4$ precursor to hollow $MnCoSe_x$/MnO@N-C nanosphere was investigated by SEM. The uniform hollow $MnCo_2O_4$ nanosphere precursor has an average diameter of 400−500 nm with a smooth surface as displayed in Fig. 2(a). After a simple selenization process, the resulting sample well maintains the initial hollow spherical morphology with the same diameter as demonstrated by the

Fig. 1 Schematic illustration for synthesis of hollow $MnCoSe_x$/MnO@N-C nanospheres

broken opening (Fig. 2(b)). After carbonization as displayed in Fig. 2(c), the hollow spherical morphology is well preserved, and the carbon layer in situ grows onto the $MnCoSe_x$/MnO. From the TEM image as displayed in Figs. 2(d, e), the obvious difference between the bright interior and black backbone demonstrates the formation of well-distributed hollow architecture, which is consistent with the SEM observations. Moreover, the HRTEM image in Fig. 2(f) presents the clearly visible well-ordered lattice fringes. Figure 2(f_1) shows the part of HRTEM image marked with box f_1 in Fig. 2(f), in which the lattice interplanar spacing of 0.19 nm can be assigned to (220) crystal planes of MnSe [23]. The clear lattice spacing of 0.27 nm in Fig. 2(f_2) is characteristic of the (101) plane of hexagonal CoSe structure [32] and the interplanar spacing of 0.22 nm in Fig. 2(f_3) is ascribed to the (200) crystal planes of MnO [11]. From Fig. 2(g), it can be observed that the amorphous carbon layer with a thickness around 15 nm was uniformly coated on the surface of $MnCoSe_x$/MnO nanosphere. Moreover, the well-distribution of Mn, Co, Se, O, C, and N elements (Figs. 2(g_1−g_6)) further confirms the successful synthesis of $MnCoSe_x$/MnO@N-C.

XRD was employed to analyze the evolution of the crystal structure and composition from hollow $MnCo_2O_4$ precursor to $MnCoSe_x$/MnO@N-C composite. As shown in Fig. 3(a), the diffraction peaks at 2θ values of 30.63°, 36.14°, 43.79°, 58.10°, and 63.79° can be ascribed to the (220), (311), (400), (511), and (440) crystal planes of the face centered cubic (fcc) structured $MnCo_2O_4$ precursor, respectively [31]. After selenization reaction, a set of discerned diffraction peaks at 2θ values of around 33.14°, 44.69°, and 50.36° can be attributed to (101), (102), and (110) planes of hexagonal CoSe, respectively [32]. Meanwhile, the diffraction peaks at 2θ values of 32.89°, 46.94°, and 58.73° can be assigned to (200), (220), and (222) planes of cubic α-MnSe, respectively [23,33]. The additional diffraction peaks located at 34.85°, 40.34°, 58.67° and 70.18° matched well with the (111), (200), (220), and (311) planes of fcc structured MnO, respectively [16]. Upon further coating the carbon shell on $MnCoSe_x$/MnO, the position of these diffraction peaks have almost no change, indicating the controlled synthesis for $MnCoSe_x$/MnO@N-C. Raman spectrum was further utilized to analyze the components of $MnCoSe_x$/MnO@N-C. Figure 3(b) exhibits two broad peaks at ~1350 and ~1580 cm^{-1} that can be assigned to the induced band (D band) and crystalline graphite band (G band) of carbon layer, representing the disordered structure and defects and the sp^2 vibration of ordered graphite

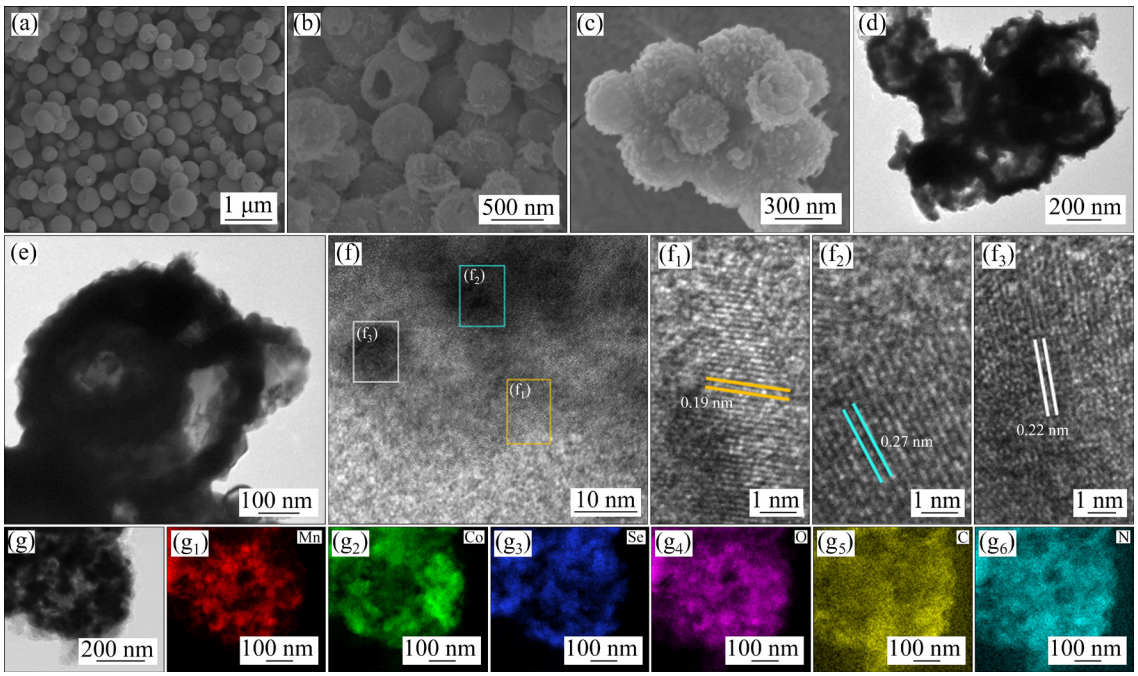

Fig. 2 SEM images of $MnCo_2O_4$ (a), $MnCoSe_x$/MnO (b), $MnCoSe_x$/MnO@N-C (c); TEM images (d, e) and HRTEM images (f, f_1−f_3) of $MnCoSe_x$/MnO@N-C; TEM element mapping of selected area of $MnCoSe_x$/MnO@N-C (g), Mn (g_1), Co (g_2), Se (g_3), O (g_4), C (g_5), and N (g_6) elements

crystals, respectively [34]. Besides, the intensity ratio of D band to G band (I_D/I_G) is approximately 1.01, demonstrating the disordered nature of the encapsulated carbon layer with high graphitization degree and abundant structural defects [35,36]. These rich defects in carbon shell could interact with the aqueous electrolytes via oxygen bonds, leading to the capacitance enhancement [36].

XPS was further executed to detect the surface elemental composition and chemical states of the hollow $MnCoSe_x$/MnO@N-C. The survey spectrum (Fig. S2 in SM) displays the existence of Mn, Co, Se, O, N, and C elements in hollow $MnCoSe_x$/MnO@N-C. In Fig. 4(a), the Mn 2p spectrum possesses two main peaks of Mn $2p_{3/2}$ at 641.6 eV and Mn $2p_{1/2}$ at 653.6 eV, and the fitted peaks at 641.6, 644.3, and 646.9 eV prove the existence of Mn^{2+}, Mn^{3+}, and Mn^{4+} valence states, respectively [33,37]. In Co 2p core level region (Fig. 4(b)), the two strong peaks at around 780.5 and 796.2 eV can be assigned into the spin-orbital doublets of Co $2p_{3/2}$ and Co $2p_{1/2}$ with shake-up satellites at 785.8 and 803.7 eV, respectively [32,38,39]. The two peaks at 54.5 and

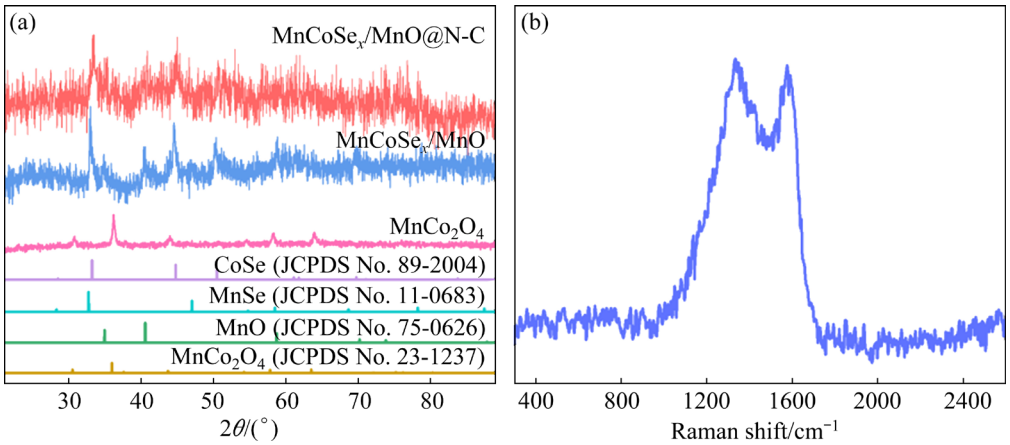

Fig. 3 XRD patterns of $MnCo_2O_4$, $MnCoSe_x$/MnO, and $MnCoSe_x$/MnO@N-C composite (a), and Raman spectrum of $MnCoSe_x$/MnO@N-C composite (b)

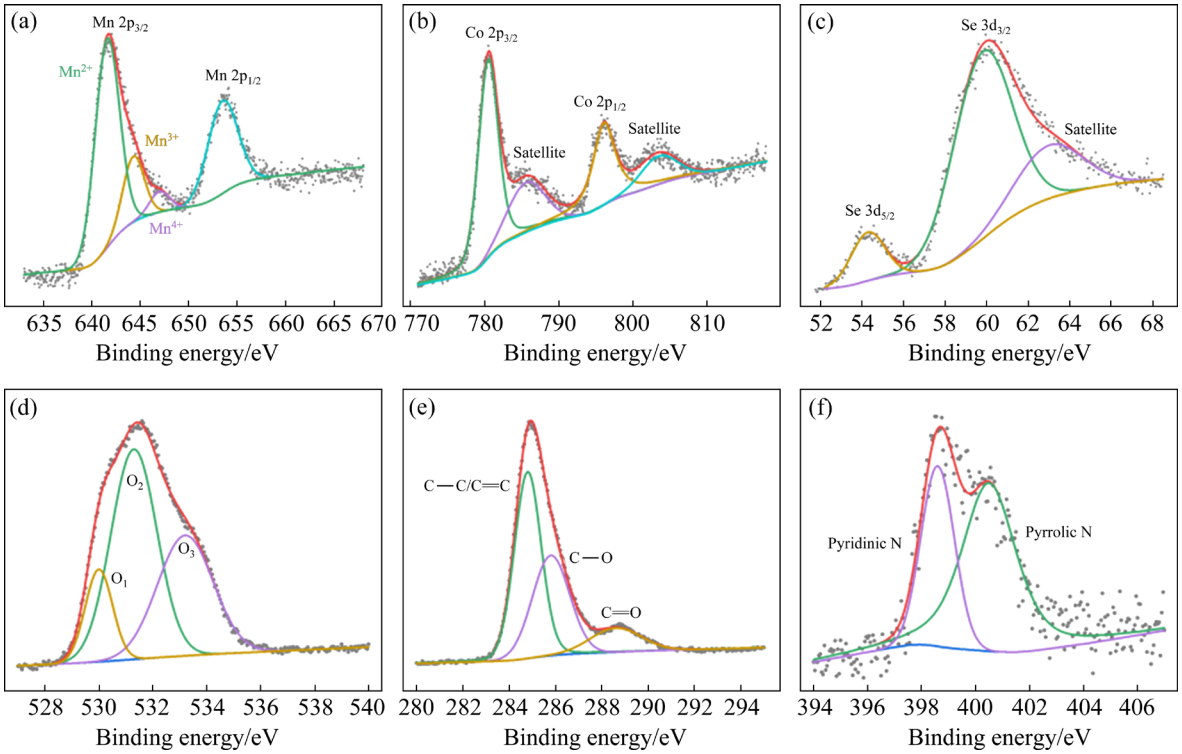

Fig. 4 XPS data and corresponding fitting data for Mn 2p (a), Co 2p (b), Se 3d (c), O 1s (d), C 1s (e), and N 1s (f) of $MnCoSe_x$/MnO@N-C

59.9 eV in Fig. 4(c) can be put down to the $3d_{5/2}$ and $3d_{3/2}$ of Se, respectively, corresponding to the typical metal−selenium bonds as reported previously [32]. The O 1s spectrum (Fig. 4(d)) shows three types contributions of O-containing species (marked as O_1 at 530.0 eV, O_2 at 531.3 eV, and O_3 at 533.1 eV), which belongs to the metal−oxygen bonds, OH species on the surfaces of $MnCoSe_x$/MnO@N-C, and oxygen vacancies, respectively [14,40]. C 1s core level region (Fig. 4(e)) can be separated into three peaks at 284.8, 285.8, and 288.6 eV, which can be assigned to the C—C/C═C, C—O, and C═O, respectively. In addition, the peak intensity of C—C/C═C bond is much stronger than that of C—O and C═O bonds, further illustrating the disordered feature of carbon in $MnCoSe_x$/MnO@N-C [22,24]. The two peaks at 398.6 and 400.5 eV (Fig. 4(f)) stem from the pyridinic N and pyrrolic N, respectively [22,34]. Additionally, the prepared $MnCoSe_x$/MnO sample (Fig. S3 in SM) also exhibited the characteristic peaks for the electronic state similar to the $MnCoSe_x$/MnO@N-C. Experimental observations above can further demonstrate that N-doped carbon shell wrapped $MnCoSe_x$/MnO composite is successfully prepared by one simple procedure.

3.2 Electrochemical properties of $MnCoSe_x$/MnO@N-C composite

The capacitive behaviors of $MnCoSe_x$/MnO@N-C were first tested by CV method at scan rates from 5 to 200 mV/s. As shown in Fig. 5(a), a couple of reversible redox peaks at 0.15 and 0.4 V indicate the typical characteristic of battery-type electrode for $MnCoSe_x$/MnO@N-C, where the possible faradaic redox reactions can be depicted as the redox couple $Mn^{2+}/Mn^{3+}/Mn^{4+}$ and $Co^{2+}/Co^{3+}/Co^{4+}$, respectively [11,20]. As the scan rate increases, the anodic peaks shift to more positive position and the cathodic peak undergoes more negative shifts due to the growing polarization at higher scan rates [23]. The CV curve still maintains its initial shape even at 200 mV/s, suggesting a brilliant rate capability

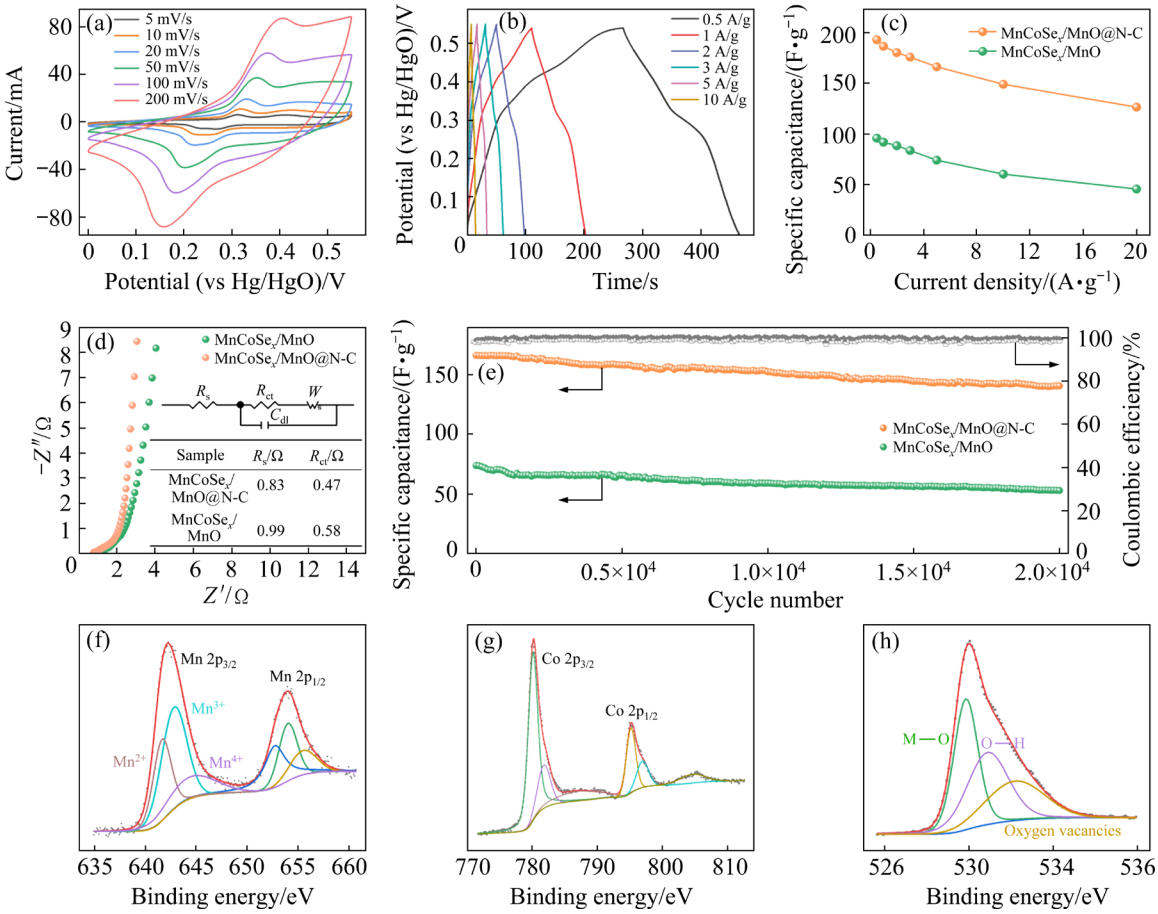

Fig. 5 Electrochemical performance of $MnCoSe_x$/MnO@N-C electrode: (a) CV curves at various scan rates; (b, c) GCD curves and specific capacitances at different current densities, respectively; (d) Nyquist plots; (e) Cycling stability at 5 A/g; (f−h) XPS patterns of $MnCoSe_x$/MnO@N-C after 20000 cycles for Mn 2p, Co 2p, and O 1s, respectively

of $MnCoSe_x$/ MnO@N-C material. For comparison, $MnCoSe_x$/MnO material was applied to CV tests under the same scan rates (Fig. S4(a) in SM), which shows smaller redox current densities and integral area than $MnCoSe_x$/MnO@N-C electrode. Figures 5(b) and S4(b) respectively display the GCD curves of $MnCoSe_x$/MnO@N-C and $MnCoSe_x$/MnO electrodes at different current densities. The observed non-linear charge−discharge curves further manifest their pseudocapacitive behavior as displayed in the CV observations. The specific capacity of $MnCoSe_x$/MnO@N-C is 193.1, 186.5, 180.4, 176.0, 166.4, 149.2, and 126.6 F/g at the current densities of 0.5, 1, 2, 3, 5, 10 and 20 A/g, respectively, which are dramatically larger than those of $MnCoSe_x$/MnO (Fig. 5(c)). About 65.6% of the capacitance for $MnCoSe_x$/MnO@N-C was reserved when the current density increased from 0.5 to 20 A/g, while it was only 47.6% for $MnCoSe_x$/MnO, further demonstrating the superior rate capability of $MnCoSe_x$/MnO@N-C. The specific capacity decay with the increase of current density should be attributed to the insufficient participation of active material in the redox reaction during the shortened charge−discharge process [41,42]. In addition, the CV curves and specific capacity of $MnCo_2O_4$ are shown in Figs. S5(a−c). It is evident that its charge storage performances were much worse than those of $MnCoSe_x$/MnO@N-C and $MnCoSe_x$/MnO electrodes. Table S1 in SM shows the performance comparison of $MnCoSe_x$/MnO@N-C electrode with other selenide materials previously reported. It can be concluded that $MnCoSe_x$/MnO@N-C possesses better specific capacitance. The elevated capacitive performances of $MnCoSe_x$/MnO@N-C could be ascribed to the following reasons. Firstly, Se owns higher electronic conductivity than O. Meanwhile, the formation of bimetallic selenides can regulate the intrinsic conductivity and provide multiple redox reaction. Moreover, the $MnCoSe_x$ and MnO phases could produce the synergetic effect for the rapid charge storage as a result of rich grain interface. Finally, the coated highly conductive N-doped carbon layer could generate the extra pseudocapacitance between the N-containing functional groups and electrolyte ions [34], and facilitate the rapid electron transfer, thereby improving the electrochemical performances of $MnCoSe_x$/MnO@N-C.

The EIS data of $MnCoSe_x$/MnO and $MnCoSe_x$/MnO@N-C electrodes are given in Fig. 5(d). In general, the semicircle in high frequency region can be assigned to the charge transfer resistance (R_{ct}) [42]. There are almost no obvious semicircles in both electrode materials, which illustrate the relatively quite small charge transfer resistances for metal selenide. The inset in Fig. 5(d) also provides the equivalent circuit mode. Here, the R_s, W, and C_{dl} represent the electrolyte resistance, Warburg impedance, and double-electric layer capacitance, respectively. As is expected, the R_s and R_{ct} values of $MnCoSe_x$/MnO@N-C (0.83 and 0.47 Ω) are smaller than those of $MnCoSe_x$/MnO (0.99 and 0.58 Ω). Based on the EIS data, it is conclusive that $MnCoSe_x$/MnO@N-C electrode owns much more electrochemical active sites and remarkable electrical conductivity. Figure 5(e) exhibits the long-term cycling stability of both electrodes during the continuous charge−discharge processes at 5 A/g. By comparison, $MnCoSe_x$/MnO@N-C exhibits superior cycling stability with 84.6% of its initial specific capacitance retained after 20000 cycles, while $MnCoSe_x$/MnO kept only 73.7%. Herein, the slight fluctuation of the specific capacitance is regarded to stem from the structural deformation and activation process of electrode material induced by the repeated charge and discharge at relatively high current density [41,42]. Moreover, the slight dissolution of the electrode material in the KOH electrolyte during the prolonged cycling also causes a part of capacity decay [41]. $MnCoSe_x$/MnO@N-C electrode also performs high coulombic efficiency (CE) around 100% over continuous tests, suggesting its excellent cycling stability. Figures S5(d, e) in SM show the corresponding data of the $MnCo_2O_4$, which were much unsatisfactory. The results above have elucidated again the superiority of the $MnCoSe_x$/MnO@N-C composite as one cathode material as compared to the $MnCoSe_x$/MnO and $MnCo_2O_4$.

We further characterize the structural evolution of $MnCoSe_x$/MnO@N-C after long term cycling. As shown in Figs. S6(a, b) in SM, the original hollow nanosphere structure well preserved after 20000 cycles, proving its good structural stability. Figures S6(c−f) in SM reveal the corresponding elements mapping images, where Mn, Co, and O

elements present uniform distribution, but the content of Se element significantly decreased compared to that for pre-cycling. XRD and XPS were further conducted to investigate the phase composition and chemical state of $MnCoSe_x$/MnO@N-C after the cycling process. As shown in Fig. S7 in SM, no peaks of CoSe and MnSe were detected, indicating the disappearance of selenides. All the peaks can be finely indexed to the mixed phases of CoOOH, MnOOH, and Mn_3O_4, which are consistent with the previous literature [43−45]. For Mn 2p signals in Fig. 5(f), the peak intensity of Mn^{3+} increased after durability measurement, while that of the Mn^{2+} greatly decreased. The Co $2p_{3/2}$ (Fig. 5(g)) shows a well-resolved peak at 780.1 eV, which can be assigned to the Co(III) species, and the much weak satellite signals confirm the absence of Co(II) species. The O 1s spectrum in Fig. 5(h) shifts to a lower binding energy, and the intensity of M—O bond increased in contrast to that of the fresh $MnCoSe_x$/MnO@N-C. The XPS data of the remaining elements are shown in Fig. S8 in SM, where the Se 3d signal is extremely weak after cycling test, which is in accordance with the observation of the EDS analysis in Fig. S9 in SM and elements mapping data mentioned above. The XRD and XPS results demonstrated that the $MnCoSe_x$/MnO@N-C sample converted to the corresponding oxides/ hydroxides through the phase transformation reactions induced by the repeated charge and discharge cycles [43−45].

3.3 Electrochemical properties of ASC based on $MnCoSe_x$/MnO@N-C

ASC devices were further assembled to estimate the practical application potential of $MnCoSe_x$/MnO@N-C material. Owing to the expanded working potential window, ASC devices own much higher storage capacitance compared with symmetric supercapacitors [8,42]. The ASC device was assembled in the 1 mol/L KOH electrolyte with the cellulose paper as a separator, the $MnCoSe_x$/MnO@N-C as a positive electrode, and AC as a negative electrode (denoted as $MnCoSe_x$/MnO@N-C//AC). The electrochemical performance of AC is shown in Fig. S10 in SM, which exhibits a typical EDLC behavior within a working potential range from −1.0 to 0 V. In order to find a stable voltage window to achieve the optimal performance of $MnCoSe_x$/MnO@N-C//AC device, diverse potential windows were measured at the same scan rate of 20 mV/s (Fig. 6(a)). It is obvious that the $MnCoSe_x$/MnO@N-C//AC remained stable at the working potential of 0−1.6 V. Therefore, the CV tests of the ASC device was conducted at various scan rates in the potential range from 0 to 1.6 V. As displayed in Fig. 6(b), the CV curves have almost identical shapes at diverse scan rates, revealing the excellent rate performance and strong charge storage reversibility for the $MnCoSe_x$/MnO@N-C//AC. In addition, unlike the electrochemical behaviors of the electrode in half cells, the $MnCoSe_x$/MnO@N-C// AC ASC clearly presents the mutual contributions from both pseudocapacitance and EDLC.

The GCD profiles of the $MnCoSe_x$/MnO@N-C//AC ASC device at different current densities in Fig. 6(c) reveal no any significant voltage drop, implying its lower intrinsic resistance. The specific capacitance of the $MnCoSe_x$/MnO@N-C//AC ASC is 35.2, 34.1, 32.8, 29.8, 26.9, 23.54, and 18.5 F/g at the current density of 0.3, 0.5, 1, 2, 3, 5 and 10 A/g, respectively (Fig. 6(d)). The capacity retention at 10 A/g is up to 53% compared to that at 0.3 A/g, indicating the excellent rate performance of the as-constructed $MnCoSe_x$/MnO@N-C//AC ASC. The long-term cycling stability was further evaluated at 3 A/g. As depicted in Fig. 6(e), the $MnCoSe_x$/MnO@N-C//AC displays a quite stable energy output with high capacity retention of about 84.0% after continuous cycling up to 20000 cycles along with the high coulombic efficiencies around 100%. The as-made $MnCoSe_x$/MnO@C//AC device possesses superior energy density and cycling stability compared to some devices constructed by other metal selenide-based electrode materials [10,17,46−50] as summarized in Table 1, which forcefully supports the practical applications of hybrid material with good electrochemical stability. The EIS data of $MnCoSe_x$/MnO@N-C//AC ASC before and after the 20000 cycles are shown in Fig. 6(f). These results have once more confirmed the superior electrochemical energy storage abilities and robust structural durability for the as-made $MnCoSe_x$/MnO@N-C electrode. To demonstrate the prospects of $MnCoSe_x$/MnO@N-C electrodes for practical applications, two fully charged $MnCoSe_x$/MnO@N-C//AC devices were assembled in series to light up LEDs of different colors and operate 18 red LEDs

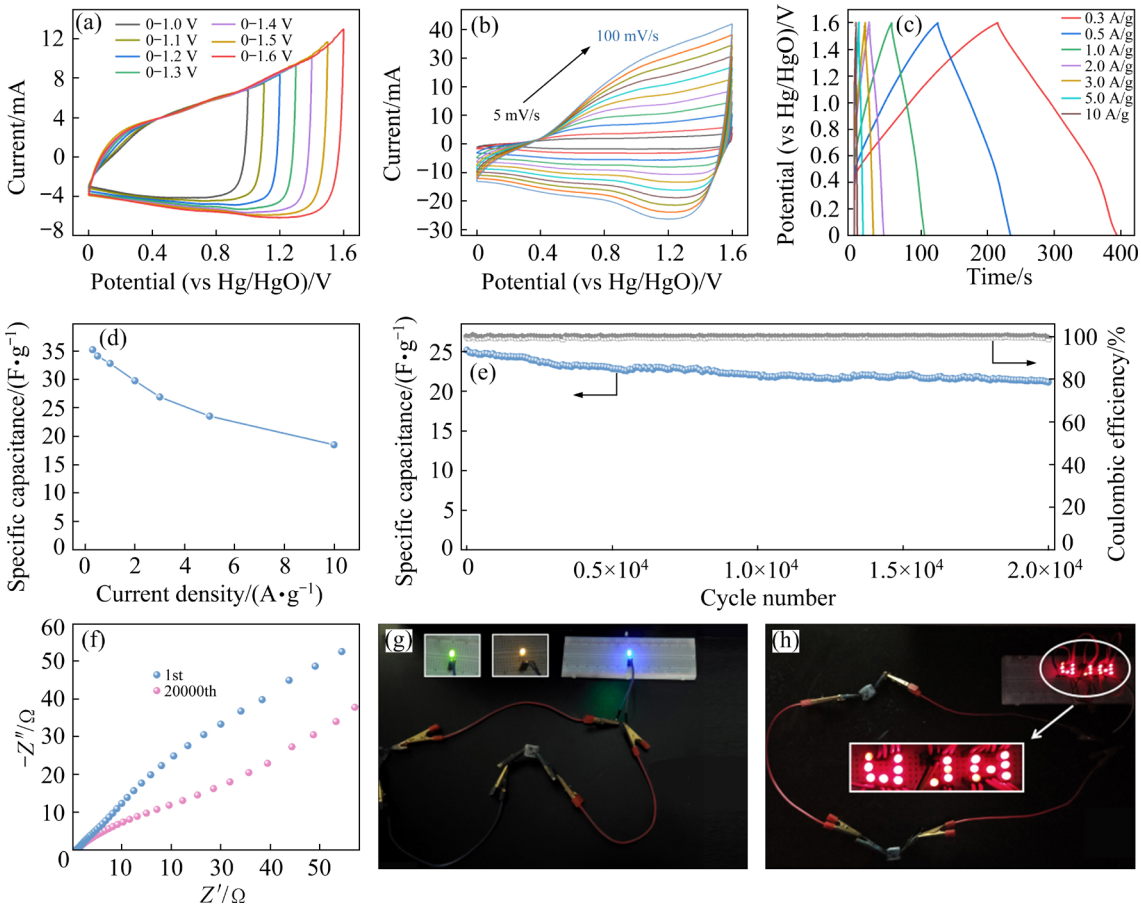

Fig. 6 Electrochemical performance of $MnCoSe_x$/MnO@N-C//AC ASC device: (a) CV curves at 20 mV/s within different potential windows; (b) CV curves at various scan rates; (c, d) GCD curves and specific capacitances at different current densities, respectively; (e) Cycling stability at 3 A/g; (f) EIS data; (g, h) LED lighting driven by two ASC devices assembled in series

Table 1 Comparison of electrochemical performances of $MnCoSe_x$/MnO@C//AC device and other devices constructed by metal selenide-based materials

Material	Energy density	Power density	Retention/%	Cycle number	Ref.
α-MnSe	2.08 W·h/kg	25 W/kg	103.4	2000	[10]
$CoSe_2$@PPy	0.08 mW·h/cm^2	0.42 mW/cm^2	80.1	15000	[17]
MnSe/$NiCo_2O_4$	12.46 W·h/kg	69.99 W/kg	86.0	5000	[46]
G-$MnSe_2$	1.84 mW·h/cm^2	19.9 mW/cm^2	75.0	4500	[47]
La_2Se_3	1.6 W·h/kg	960 W/kg	80.0	1000	[48]
$(NiCo)_{0.85}Se$	12.5 W·h/kg	112.5 W/kg	85.0	10000	[49]
$Co_{0.85}Se$	14.2 W·h/kg	400 W/kg	93.8	5000	[50]
$MnCoSe_x$/MnO@N-C	11.2 W·h/kg	810 W/kg	84.0	20000	This work

assembled into a UJN symbol as shown in Figs. 6(g, h). Accordingly, the $MnCoSe_x$/MnO@N-C//AC ASC device shows promising application potential as the rechargeable microelectronic devices.

$MnCoSe_x$/MnO@N-C exhibits superior charge storage performances with high reversible capacitance and prolonged cycling stability. It is considered that its outstanding electrochemical performances benefit from the carefully designed unique composition and structure. On the one hand, the interface coupling between bimetallic selenides

and oxide composites can share and combine their individual electronic features together to provide multiple redox activity, boost electronic conductivity, and improve the rate performances in the charge storage process. On the other hand, the large internal voids in the nanospheres can furnish abundant active sites and shorten the ion/electron delivery path, thereby achieving large capacity and high rate performance. In addition, the robust protective N-doped carbon shell coated on the surface of the $MnCoSe_x$/MnO can not only further enhance its electrical conductivity but also help to relieve the structural damage and strengthen the structure stability during the repeated charge and discharge processes, thus ensuring the enhanced cycling stability.

4 Conclusions

(1) The uniform hollow $MnCoSe_x$/MnO@N-C nanospheres with the rich specific surface area and robust protective carbon shell were easily prepared.

(2) $MnCoSe_x$/MnO@N-C shows extraordinary charge storage performances in terms of high specific capacitance, remarkable cycling stability, and outstanding rate capability due to the unique structural merits and the enhanced electronic conductivity.

(3) The as-constructed ASC device possesses high power and energy density, exceptional rate capability, and excellent cycling stability.

(4) With the advantages of these impressive performances, the as-prepared $MnCoSe_x$/MnO@N-C holds prospective application potential as a cathode candidate for electrochemical energy storage.

Acknowledgments

This work was supported by the National Natural Science Foundation of China (No. 51772133), the Taishan Scholar Project of Shandong Province, China (ZR2017JL022), the Project of “20 Items of University” of Jinan, China (No. 2018GXRC001), and Case-by-Case Project for Top Outstanding Talents of Jinan, China.

Supplementary Materials

Supplementary Materials in this paper can be found at: http://tnmsc.csu.edu.cn/download/18-p2471-2022-0270-Supplementary_Materials.pdf.

References

[1] LIU Yang, SUN Ze-hang, TAN Ke, DENIS D K, SUN Jin-feng, LIANG Long-wei, HOU Lin-rui, YUAN Chang-zhou. Recent progress in flexible non-lithium based rechargeable batteries [J]. Journal of Materials Chemistry A, 2019, 7: 4353−4382.

[2] LIU Yang, SUN Ze-hang, SUN Xuan, LIN Yue, TAN Ke, SUN Jin-feng, LIANG Long-wei, HOU Lin-rui, YUAN Chang-zhou. Construction of hierarchical nanotubes assembled from ultrathin V_3S_4@C nanosheets towards alkali-ion batteries with ion-dependent electrochemical mechanisms [J]. Angewandte Chemie, 2020, 59: 2473−2482.

[3] MA Bei-bei, CHEN Shui-jiao, HUANG Ye-wei, NIE Zhen-zhen, QIU Xiao-bin, XIE Xiu-qiang, WU Zhen-jun. Electrochemical lithium storage performance of three-dimensional foam-like biocarbon/MoS_2 composites [J]. Transactions of Nonferrous Metals Society of China, 2021, 31: 255−264.

[4] XU Yong-tai, FENG Jian-ze, MA Hong-yun, ZHU Jiao-jiao, ZHANG Xu, LANG Jun-wei, YANG Sheng-rong, YAN Xing-bin. Superior volumetric capability dual-ion batteries enabled by a microsize niobium tungsten oxide anode [J]. Advanced Functional Materials, 2022, 32: 2112223.

[5] LI Fang-cheng, ZHANG Gang, ZHANG Zong-liang, YANG Jian, LIU Fang-yang, JIA Ming, JIANG Liang-xing. Regeneration of Al-doped $LiNi_{0.5}Co_{0.2}Mn_{0.3}O_2$ cathode material by simulated hydrometallurgy leachate of spent lithium-ion batteries [J]. Transactions of Nonferrous Metals Society of China, 2022, 32: 593−603.

[6] DEEPI A S, NESARAJ A S. Design of best performing hexagonal shaped Ag@CoS/rGO nanocomposite electrode material for electrochemical supercapacitor application [J]. Transactions of Nonferrous Metals Society of China, 2020, 30: 2764−2774.

[7] ZHU Hang-tian, LI Ling-yun, SHI Min-jie, XIAO Peng, LIU Yu-ting, YAN Xing-bin. Coupling of graphene quantum dots with MnO_2 nanosheets for boosting capacitive storage in ionic liquid electrolyte [J]. Chemical Engineering Journal, 2022, 437: 135301.

[8] HOU Lin-rui, SHI Yao-yao, WU Chen, ZHANG Yan-ru, MA Yang-zhou, SUN Xuan, SUN Jin-feng, ZHANG Xiao-gang, YUAN Chang-zhou. Monodisperse metallic $NiCoSe_2$ hollow sub-microspheres: Formation process, intrinsic charge-storage mechanism, and appealing pseudocapacitance as highly conductive electrode for electrochemical supercapacitors [J]. Advanced Functional Materials, 2018, 28: 1705921.

[9] HUANG Qi, LIU Kai-yu, HE Fang, ZHANG Shui-rong, XIE Qing-liang, CHEN Cheng. Fabrication of cobalt aluminum-layered double hydroxide nanosheets/carbon spheres composite as novel electrode material for supercapacitors [J]. Transactions of Nonferrous Metals Society of China, 2017, 27: 1804−1814.

[10] SAHOO S, PAZHAMALAI P, KRISHNAMOORTHY K, KIM S J. Hydrothermally prepared α-MnSe nanoparticles as a new pseudocapacitive electrode material for supercapacitor [J]. Electrochimica Acta, 2018, 268: 403−410.

[11] RAMADAN M, ABDELLAH A M, MOHAMED S G, ALLAM N K. 3D interconnected binder-free electrospun

MnO@C nanofibers for supercapacitor devices [J]. Scientific Reports, 2018, 8: 7988.

[12] ZHAI Teng, WAN Li-ming, SUN Shuo, CHEN Qi, SUN Jiao, XIA Qiu-ying, XIA Hui. Phosphate ion functionalized Co_3O_4 ultrathin nanosheets with greatly improved surface reactivity for high performance pseudocapacitors [J]. Advanced Materials, 2017, 29: 1604167.

[13] YANG Hong-zhi, ZOU Jian-peng. Controllable preparation of hierarchical NiO hollow microspheres with high pseudo-capacitance [J]. Transactions of Nonferrous Metals Society of China, 2018, 28: 1808−1818.

[14] ARUL N S, HAN J I. Enhanced pseudocapacitance of $NiSe_2/Ni(OH)_2$ nanocomposites for supercapacitor electrode [J]. Materials Letters, 2019, 234: 87−91.

[15] CAI Qi-fa, LI Yuan-yuan, WANG Lei, LI Qing-wei, XU Juan, GAO Biao, ZHANG Xu-ming, HUO Kai-fu, CHU P K. Freestanding hollow double-shell $Se@CN_x$ nanobelts as large-capacity and high-rate cathodes for Li−Se batteries [J]. Nano Energy, 2017, 32: 1−9.

[16] AMIN B G, MASUD J, NATH M. Facile one-pot synthesis of $NiCo_2Se_4$-rGO on Ni foam for high performance hybrid supercapacitors [J]. RSC Advances, 2019, 9: 37939−37946.

[17] WANG Qiu-fan, MA Yun, LIANG Xiao, ZHANG Dao-hong, MIAO Meng-he. Novel core/shell $CoSe_2$@PPy nanoflowers for high-performance fiber asymmetric supercapacitors [J]. Journal of Materials Chemistry A, 2018, 6: 10361−10369.

[18] LIU Xiao-bin, LIU Yong-chang, FENG Ming, FAN Li-zhen. MOF-derived and nitrogen-doped ZnSe polyhedra encapsulated by reduced graphene oxide as the anode for lithium and sodium storage [J]. Journal of Materials Chemistry A, 2018, 6: 23621−23627.

[19] PENG Hui, WEI Chun-ding, WANG Kai, MENG Tian-yu, MA Guo-fu, LEI Zi-qiang, GONG Xiong. $Ni_{0.85}Se@MoSe_2$ nanosheet arrays as the electrode for high-performance supercapacitors [J]. ACS Applied Materials & Interfaces, 2017, 9: 17067−17075.

[20] SAKTHIVEL M, RAMARAJ S, CHEN S M, HO K C. Bimetallic vanadium cobalt diselenide nanosheets with additional active sites for excellent asymmetric pseudo-capacitive performance: Comparing the electro- chemical performances with M-$CoSe_2$ (M = Zn, Mn, and Cu) [J]. Journal of Materials Chemistry A, 2019, 7: 12565−12581.

[21] LIN Jing-huang, WANG Hao-han, YAN Yao-tian, ZHENG Xiao-hang, JIA He-nan, QI Jun-lei, CAO Jian, TU Jin-chun, FEI Wei-dong, FENG Ji-cai. Core-branched $CoSe_2/Ni_{0.85}Se$ nanotube arrays on Ni foam with remarkable electrochemical performance for hybrid supercapacitors [J]. Journal of Materials Chemistry A, 2018, 6: 19151−19158.

[22] LIU Qiang, HOU Jia-gang, HAO Qin, HUANG Peng, XU Cai-xia, ZHOU Qiu-xia, ZHOU Ji, LIU Hong. Nitrogen-doped carbon encapsulated hollow ZnSe/$CoSe_2$ nanospheres as high performance anodes for lithium-ion batteries [J]. Nanoscale, 2020, 12: 22778−22786.

[23] TANG Hai-chao, YUAN Yu-liang, MENG Lu, WANG Wei-cheng, LU Jian-guo, ZENG Yu-jia, HUANG Tie-qi, GAO Chao. Low-resistance porous nanocellular MnSe electrodes for high-performance all-solid-state battery-supercapacitor hybrid devices [J]. Advanced Materials Technologies, 2018, 3: 1800074.

[24] CHEN Zi-zhong, HOU Jia-gang, ZHOU Ji, HUANG Peng, WANG Hai-qing, XU Cai-xia. Carbon shell coated hollow $NiCoSe_x$ composite as high-performance anode for lithium storage [J]. Rare Metals, 2021, 40: 3185−3194.

[25] LI Yan-juan, WANG Min, LIU Sa, GAO Jing-xia, YANG Shun, LIU Zi-hao, LAI Xiao-yong, YAN Xiao. Preparation and properties of transition metal nitrides caged in N-doped hollow porous carbon sphere for oxygen reduction reaction [J]. Transactions of Nonferrous Metals Society of China, 2021, 31: 1427−1438.

[26] LAI Xiao-yong, HALPERT J E, WANG D. Recent advances in micro-/nano-structured hollow spheres for energy applications: From simple to complex systems [J]. Energy & Environmental Science, 2012, 5: 5604−5618.

[27] YANG Fu-hua, ZHANG Zhi-an, HAN Yu, DU Ke, LAI Yan-qing, LI Jie. TiO_2/carbon hollow spheres as anode materials for advanced sodium ion batteries [J]. Electrochimica Acta, 2015, 178: 871−876.

[28] XIN Xi-peng, SONG Na, JIA Rui-ming, WANG Bing-nan, DONG Hong-zhou, MA Shuai, SUI Li-na, CHEN Ying-jie, ZHANG Qian, DONG Li-feng, YU Li-yan. N, P-codoped porous carbon derived from chitosan with hierarchical N-enriched structure and ultra-high specific surface area toward high-performance supercapacitors [J]. Journal of Materials Science & Technology, 2021, 88: 45−55.

[29] JIA Miao, JIN Yu-hong, ZHAO Pei-zhu, ZHAO Chen-chen, JIA Meng-qiu, WANG Li, HE Xiang-ming. Hollow $NiCoSe_2$ microspheres@N-doped carbon as high-performance pseudo-capacitive anode materials for sodium ion batteries [J]. Electrochimica Acta, 2019, 310: 230−239.

[30] LOU Xiong-wen, ARCHER L A, YANG Zi-chao. Hollow micro-/nanostructures: Synthesis and applications [J]. Advanced Materials, 2008, 20: 3987−4019.

[31] WANG Meng-yi, YU Xing, HOU Long, GAGNOUD A, FAUTRELLE Y, MOREAU R, LI Xi. 3D sandwich-shaped graphene-based nanocomposite intercalated with double-shelled hollow $MnCo_2O_4$ spheres as anode materials for lithium-ion batteries [J]. Chemical Engineering Journal, 2018, 351: 930−938.

[32] ZHU Yi-rong, HUANG Zhao-dong, HU Zhong-liang, XI Liu-jiang, JI Xiao-bo, LIU Yong. 3D interconnected ultrathin cobalt selenide nanosheets as cathode materials for hybrid supercapacitors [J]. Electrochimica Acta, 2018, 269: 30−37.

[33] JAVED M S, SHAH S S A, HUSSAIN S, TAN Shao-zao, MAI Wen-jie. Mesoporous manganese-selenide micro-flowers with enhanced electrochemical performance as a flexible symmetric 1.8 V supercapacitor [J]. Chemical Engineering Journal, 2020, 382: 122814.

[34] CAI Ning, FU Jing, CHAN V, LIU Ming-ming, CHEN Wei-min, WANG Jian-zhi, ZENG Huan, YU Fa-quan. $MnCo_2O_4$@nitrogen-doped carbon nanofiber composites with meso-microporous structure for high-performance symmetric supercapacitors [J]. Journal of Alloys and Compounds, 2019, 782: 251−262.

[35] LIU Yong-chang, ZHANG Ning, YU Chuan-ming, JIAO Li-fang, CHEN Jun. $MnFe_2O_4$@C nanofibers as high-performance anode for sodium-ion batteries [J]. Nano Letters, 2016, 16: 3321−3328.

[36] MOUSSA G, MATEI GHIMBEU C, TABERNA P L, SIMON P, VIX-GUTERL C. Relationship between the carbon nano-onions (CNOs) surface chemistry/defects and their capacitance in aqueous and organic electrolytes [J]. Carbon, 2016, 105: 628−637.

[37] ZHOU Peng, CHEN Li-bao, ZHANG Ming-yu, HUANG Qi-zhong, CUI Chao, LI Xiu, WANG Li-ping, LI Lie-wu, YANG Cheng, LI Yu-hao. Embedding *α*-MnSe nanodots in nitrogen-doped electrospinning carbon nanofibers to enhanced storage properties of lithium-ion batteries [J]. Journal of Alloys and Compounds, 2019, 797: 826−833.

[38] SHI Xin, WANG Hui, JI Shan, LINKOV V, LIU Fu-sheng, WANG Rong-fang. $CoNiSe_2$ nanorods directly grown on Ni foam as advanced cathodes for asymmetric supercapacitors [J]. Chemical Engineering Journal, 2019, 364: 320−327.

[39] CHEN Hai-chao, CHEN Si, FAN Mei-qiang, LI Chao, CHEN Da, TIAN Guang-lei, SHU Kang-ying. Bimetallic nickel cobalt selenides: A new kind of electroactive material for high-power energy storage [J]. Journal of Materials Chemistry A, 2015, 3: 23653−23659.

[40] SAKTHIVEL M, SUKANYA R, CHEN S M, PANDI K, HO K C. Synthesis and characterization of bimetallic nickel-cobalt chalcogenides ($NiCoSe_2$, $NiCo_2S_4$, and $NiCo_2O_4$) for non-enzymatic hydrogen peroxide sensor and energy storage: Electrochemical properties dependence on the metal-to-chalcogen composition [J]. Renewable Energy, 2019, 138: 139−151.

[41] JIAN Tian-zhen, ZHU Jin-yun, MA Wen-qing, YAN Xiu-ling, LI Guang-da, ZHOU Jian-hua. Interconnected two-dimensional MnO_2 nanosheets anchored on three-dimensional porous Cu skeleton as a high-performance cathode for energy storage [J]. Applied Surface Science, 2020, 529: 147152.

[42] LIU Bin-bin, HOU Jia-gang, ZHANG Ting-ting, XU Cai-xia, LIU Hong. A three-dimensional multilevel nanoporous $NiCoO_2$/Ni hybrid for highly reversible electrochemical energy storage [J]. Journal of Materials Chemistry A, 2019, 7: 16222−16230.

[43] RAMAN V, CHINNADURAI D, RAJMOHAN R, CHEBROLU V T, RAJANGAM V, KIM H J. Transition metal chalcogenide based MnSe heterostructured with $NiCo_2O_4$ as a new high performance electrode material for capacitive energy storage [J]. New Journal of Chemistry, 2019, 43: 12630−12640.

[44] BALAMURALITHARAN B, KARTHICK S N, BALASINGAM S K, HEMALATHA K V, SELVAM S, RAJ J A, PRABAKAR K, JUN Y, KIM H J. Hybrid reduced graphene oxide/manganese diselenide cubes: A new electrode material for supercapacitors [J]. Energy Technology, 2017, 5: 1953−1962.

[45] XIE Sheng-li, GOU Jian-xia, LIU Bin, LIU Chen-guang. Nickel−cobalt selenide as high-performance and long-life electrode material for supercapacitor [J]. Journal of Colloid and Interface Science, 2019, 540: 306−314.

[46] WANG Yin, YANG Yu-tong, WANG Xia, LI Pei-he, SHAO Hong-yang, LI Tian-en, LIU Hai-yang, ZHENG Qing-fu, HU Jing, DUAN Li-mei, HU Chang-wen, LIU Jing-hai. Electro-synthesized $Co(OH)_2$@CoSe with Co−OH active sites for overall water splitting electrocatalysis [J]. Nanoscale Advances, 2020, 2: 792−797.

[47] SUN Mao, GAO Rui-ting, LIU Xian-hu, GAO Rui, WANG Lei. Manganese-based oxygen evolution catalysts boosting stable solar-driven water splitting: MnSe as an intermetallic phase [J]. Journal of Materials Chemistry A, 2020, 8: 25298−25305.

[48] PATIL S J, BULAKHE R N, LOKHANDE C D. Nanoflake-modulated La_2Se_3 thin films prepared for an asymmetric supercapacitor device [J]. Chempluschem, 2015, 80: 1478−1487.

[49] XIA Chuan, JIANG Qiu, ZHAO Chao, BEAUJUGE P M, ALSHAREEF H N. Asymmetric supercapacitors with metal-like ternary selenides and porous graphene electrodes [J]. Nano Energy, 2016, 24: 78−86.

[50] PENG Hui, MA Guo-fu, SUN Kan-jun, ZHANG Zhi-guo, LI Jin-dan, ZHOU Xiao-zhong, LEI Zi-qiang. A novel aqueous asymmetric supercapacitor based on petal-like cobalt selenide nanosheets and nitrogen-doped porous carbon networks electrodes [J]. Journal of Power Sources, 2015, 297: 351−358.

多界面耦合空心核壳 $MnCoSe_x$/MnO@氮掺杂碳复合材料的制备及电化学性能

周 济[1]，张丽娜[2]，刘彬彬[1]，徐彩霞[1]，刘 宏[1,3]

1. 济南大学 前沿交叉科学研究院(iAIR)，济南 250022；
2. 济南大学 山东省建筑材料制备与测试技术重点实验室，济南 250022；
3 山东大学 晶体材料国家重点实验室，济南 250100

摘 要：通过简单的溶剂热和硒化策略以及进一步的碳层包覆程序制备氮掺杂碳壳包裹的空心 $MnCoSe_x$/MnO 纳米球($MnCoSe_x$/MnO@N-C)。得益于 $MnCoSe_x$ 和 MnO 之间的多界面耦合以及独特的空心核壳结构，$MnCoSe_x$/MnO@N-C 复合材料具有较高的比电容和优异的倍率性能，即使在 5 A/g 的高电流密度下，$MnCoSe_x$/MnO@N-C 仍可以稳定运行 20000 次循环，并保持 84.6%的初始比电容。由 $MnCoSe_x$/MnO@N-C 和活性炭组装的非对称超级电容器器件在功率密度为 810 W/kg 时表现出 11.2 W·h/kg 的高能量密度，并拥有超长的循环寿命，在 20000 次循环后仍可保留初始比电容的 84.0%。

关键词：硒化物；空心纳米球；氮掺杂碳；正极；超级电容器；电化学性能

(Edited by Wei-ping CHEN)